

First Principles Study of the Giant Magnetic Anisotropy Energy in Bulk Na_4IrO_4

Di Wang¹, Feng Tang¹, Yongping Du^{2,1}, and Xiangang Wan^{1*}

¹*National Laboratory of Solid State Microstructures and Department of Physics, Nanjing University, Nanjing 210093, China*

²*Department of Applied Physics, Nanjing University of Science and Technology, Nanjing 210094, China*

(Dated: March 7, 2024)

In $5d$ transition metal oxides, novel properties arise from the interplay of electron correlations and spin-orbit interactions. Na_4IrO_4 , where $5d$ transition-metal Ir atom occupies the center of the square-planar coordination environment, is synthesized. Based on density functional theory, we calculate its electronic and magnetic properties. Our numerical results show that the Ir- $5d$ bands are quite narrow, and the bands around the Fermi level are mainly contributed by d_{xy} , d_{yz} and d_{zx} orbitals. The magnetic easy-axis is perpendicular to the IrO_4 plane, and the magnetic anisotropy energy (MAE) of Na_4IrO_4 is found to be very giant. We estimate the magnetic parameters by mapping the calculated total energy for different spin configurations onto a spin model. The next nearest neighbor exchange interaction J_2 is much larger than other intersite exchange interactions and results in the magnetic ground state configuration. Our study clearly demonstrates that the huge MAE comes from the single-ion anisotropy rather than the anisotropic interatomic spin exchange. This compound has a large spin gap but very narrow spin-wave dispersion, due to the large single-ion anisotropy and relatively small exchange couplings. Noticing this remarkable magnetic feature originated from its highly isolated IrO_4 moiety, we also explore the possibility to further enhance the MAE.

I. INTRODUCTION

It is well known that the Coulomb interaction is of substantial importance in $3d$ electron systems, while the spin-orbit coupling (SOC) in these compounds is quite small [1, 2]. However, the SOC and electronic correlation in $5d$ electrons have comparable magnitudes. The delicate interplay between electronic interactions, strong SOC, and crystal field splitting can result in strongly competing ground states in these materials [3–5]. Thus recently, $5d$ transition metal (especially Ir or Os) oxides have attracted intensive interest and a great number of exotic phenomena have been observed experimentally or proposed theoretically, e.g. $J_{eff}=1/2$ Mott state [6–8], topological insulator [9–11], Kitaev model [12], Weyl Semimetal [13], high T_c superconductivity [14], Axion insulator [15], quantum spin liquid [16, 17], Slater insulator [18–20], ferroelectric metal [21, 22], etc.

In all the aforementioned systems, the $5d$ ions lie in the octahedral environment of the O ions. In addition to this common coordination geometry, Na_4IrO_4 , where Ir atom occupies the center of the square-planar coordination environment, has also been synthesized [24]. By using density function theory (DFT) calculations, Kanungo [25] *et al.* reveal that the relative weak Coulomb repulsion of Ir ions plays a key role in the stabilization of the ideal square-planar geometry of the IrO_4 moiety in Na_4IrO_4 . Located at the center of an ideally square-planar IrO_4 oxoanion, the $5d$ electrons of Ir ions in Na_4IrO_4 do not display the $J_{eff}=1/2$ configuration [25]. Moreover, the common $5d$ transition metal oxides own face (or edge, corner)-sharing structure of oxygen octahedrons, while

the square-planar IrO_4 oxoanion in Na_4IrO_4 is quite isolated. Therefore, exploring the possible exotic properties of Na_4IrO_4 is an interesting study.

In this work, based on first principle calculations, we systematically study the electronic and magnetic properties of Na_4IrO_4 . Our numerical results show that the Ir- $5d$ bands are quite narrow, and the bands around the Fermi level are mainly contributed by d_{xy} , d_{yz} and d_{zx} orbitals. Due to the isolated IrO_4 moiety, the magnetic moments are quite localized. We calculate several magnetic structures and find that the antiferromagnetic-1 (AFM-1) state as shown in Fig. 4 is the ground state configuration. The interatomic exchange interactions are estimated and the nearest-neighbor J_2 (shown in Fig. 1) dominates over the others. We find that there is a huge magnetic anisotropy energy (MAE) due to the special square-planar coordination environment and the long distance between IrO_4 moieties. We find the anisotropy of interatomic spin exchange couplings is relatively small, and the huge MAE comes from the single-ion anisotropy. We suggest that substituting Ir by Re atom can further enhance the MAE significantly.

II. METHOD AND CRYSTAL STRUCTURE

The electronic band structure and density of states calculations have been carried out by using the full potential linearized augmented plane wave method as implemented in Wien2k package [26]. Local spin density approximation (LSDA) is widely used for various $4d$ and $5d$ TMOs [6, 7, 13, 15, 27], and we therefore adopt it as the exchange-correlation potential. A $9 \times 9 \times 15$ k-point mesh is used for the Brillouin zone integral. Using the second-order variational procedure, we include the SOC [28], which has been found to play an important role in

*Corresponding author: xgwan@nju.edu.cn

the $5d$ system. The self-consistent calculations are considered to be converged when the difference in the total energy of the crystal does not exceed 0.01 mRy. Despite the fact that the $5d$ orbitals are spatially extended, recent theoretical and experimental work has given evidence on the importance of Coulomb interactions in $5d$ compounds [3–5]. We utilize the LSDA + U scheme [29] to take into account the effect of Coulomb repulsion in $5d$ orbital. We vary the parameter U between 2.0 and 3.0 eV and find that the essential properties are independent on the value of U .

As shown in Fig. 1, Na_4IrO_4 crystallizes in the tetragonal structure (space group $I4/m$) [24]. The lattice constants of Na_4IrO_4 are $a = 7.17$ Å and $c = 4.71$ Å [24]. There is only one formula unit in the primitive unit cell, and the nine atoms in the unit cell are located at three nonequivalent crystallographic sites: Ir atoms occupy the $2a$ position: $(0,0,0)$, while both Na and O reside at the $8h$ sites: (x,y,z) [24]. The square-planar IrO_4 oxoanion occurs in the ab -plane, and is slightly rotated about the c axis [24]. The Ir ions occupy the center of the square-planar coordination environment. The average distance of four Ir-O bonds in the square-planar IrO_4 is 1.91 Å, which is similar to the Ir-O bond length in IrO_6 octahedron. Instead of the face (or edge, corner)-sharing structure of octahedrons, the IrO_4 moiety is quite isolated as shown in Fig. 1, thus the Ir-Ir distance is quite large. These remarkable structural features significantly affect the electronic structure and magnetic properties of Na_4IrO_4 as shown in the following sections.

III. BAND STRUCTURES

To clarify the basic electronic features, we perform nonmagnetic LDA calculation, and show the band structures and the density of states (DOS) in Fig. 2(a) and Fig. 3, respectively. As shown in Fig. 3, that O- $2p$ states are mainly located between -7.0 and -1.0 eV while the Na $3s$ and $3p$ bands appear mainly above 3.0 eV which is much higher than the Fermi level and also appear between -7.0 and -1.0 eV contributed mainly by the O- $2p$ states, indicating the non-negligible hybridization between Na and O states despite that Na is highly ionic. Hence the chemical valence for Na is +1 while that for O is -2. As a result, the nominal valence of Ir in Na_4IrO_4 is +4, and the electronic configuration of Ir ion is $5d^5$. It is well known that in the octahedral environment the $5d$ orbitals will split into the t_{2g} and e_g states, and the strong SOC in $5d$ electrons splits the t_{2g} states into $J_{eff} = 1/2$ and $J_{eff} = 3/2$ bands [6, 7]. Compared with the IrO_6 octahedra, the upper and lower O^{2-} ions are absent in the square-planar IrO_4 oxoanion. Consequently the Ir- $5d$ orbitals split into three non-degenerate orbitals: $d_{3z^2-r^2}$, d_{xy} , $d_{x^2-y^2}$, and doubly degenerate d_{xz}/d_{yz} ones. There are in total 13 bands in the energy range from -7.0 eV to -1.0 eV, as shown in Fig. 2(a). The $d_{3z^2-r^2}$ states appear mainly between -3.0 eV to -2.0 eV,

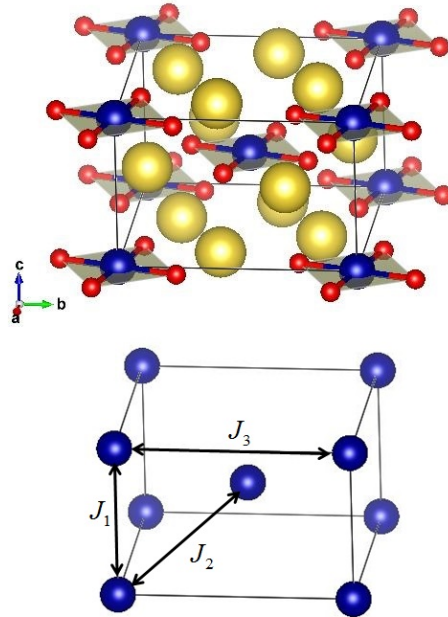


FIG. 1: Crystal structure of Na_4IrO_4 . The yellow, blue, and red balls represent the Na, Ir, and O ions, respectively. The nearest-neighbor, next-nearest-neighbor and third-nearest-neighbor exchange interactions for Ir magnetic moments are shown by J_1 , J_2 , J_3 respectively, which are the parameters in the Heisenberg model $H = \sum_{i<j} J_{ij} S_i \cdot S_j$.

while the remaining 12 bands are contributed by O- $2p$ states. Mainly located above 4 eV, $d_{x^2-y^2}$ states have also large distribution around -6.5 eV due to the strong hybridization with O- $2p$ bands. The d_{xz}/d_{yz} and d_{xy} orbitals are mainly located from -1.0 to 1.0 eV, while the d_{xy} state is slightly higher in energy. As shown in Fig. 2(a) and Fig. 3, these bands are separated from other bands, and around the Fermi level the orbital splitting can be displayed by the left panel of Fig. 6. The dispersion of the $5d$ bands around Fermi level is very narrow, due to that the IrO_4 moiety is quite isolated in the crystal structure. As shown in Fig. 3, the DOS at Fermi level is rather high, which indicates the magnetic instability.

To understand the magnetic properties, we also perform a spin polarized calculation and show the band structures of ferromagnetic (FM) configuration in Fig. 2(b) and 2(c). Basically, the $d_{3z^2-r^2}$ states are fully occupied while the $d_{x^2-y^2}$ ones are empty, and the spin polarization has a relatively small effect on these bands. On the other hand, the partially occupied d_{xz}/d_{yz} and d_{xy} states are significantly affected, and these bands have about 1 eV exchange splitting, as shown in Fig. 2(b) and 2(c). LSDA calculation for FM configuration gives a insulating solution with a band gap of 0.16 eV. Experiment reveals that Na_4IrO_4 has a long-range antifer-

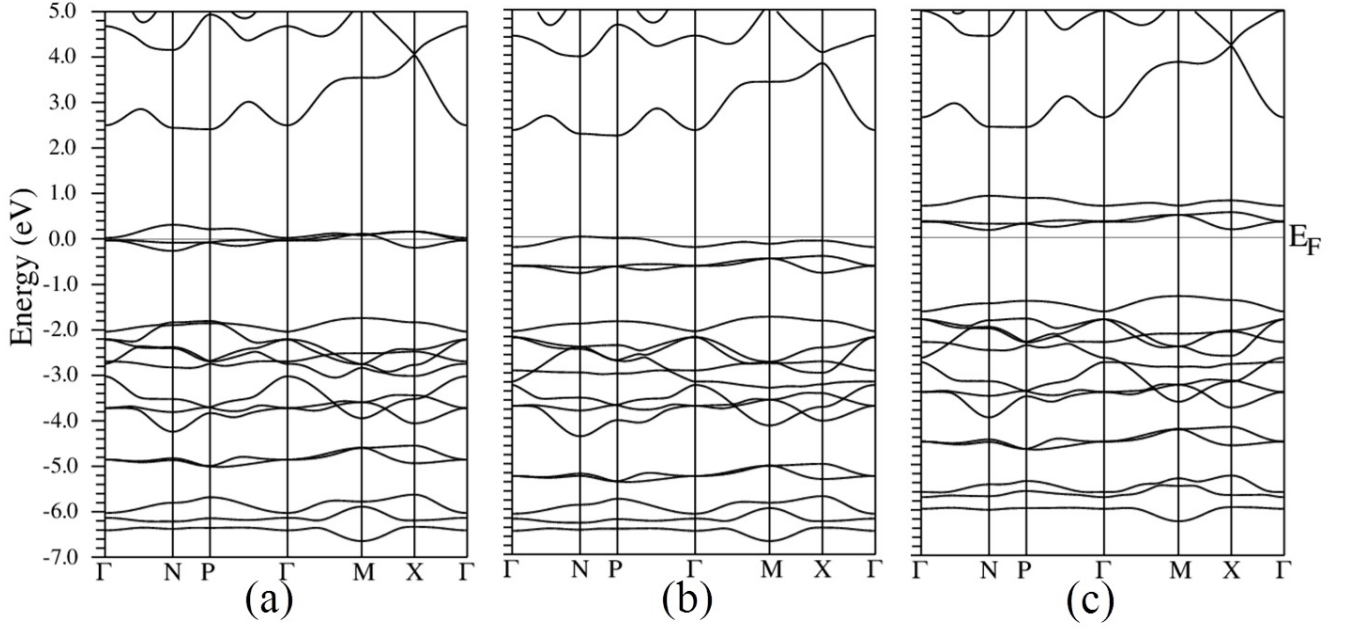


FIG. 2: Band structures of Na_4IrO_4 . (a) represents the LDA calculation while (b) and (c) represent spin-up and spin-down channel from LSDA calculation with FM configuration. The Fermi energy is set to zero.

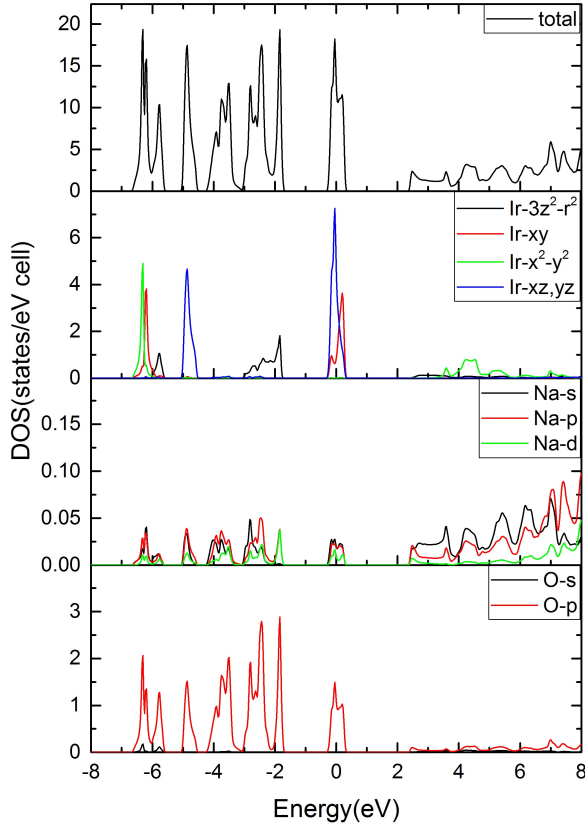


FIG. 3: Partial density of states (PDOS) of Na_4IrO_4 calculated by the method of LDA calculation. The Fermi energy is set to zero.

romagnetic (AFM) order at low temperature [25]. Thus we also explore the magnetic configuration. In addition to the FM configuration, we also consider three AFM states: AFM-1 where Ir atoms at the body center and corners have opposite spin orientations, AFM-2 where Ir atoms couple anti-ferromagnetically along a-axis, AFM-3 where Ir atoms couple anti-ferromagnetically along c-axis (See Fig. 4 for the magnetic structures of different AFM configurations). The relative total energies and magnetic moments for the four magnetic configurations are summarized in Table. I. Different magnetic configurations have similar calculated magnetic moments. This indicates that the magnetism in Na_4IrO_4 is quite localized. The distance between IrO_4 oxoanion is quite large as shown in Fig. 1, thus the effective hopping between Ir ions in Na_4IrO_4 is very weak. As a result, the magnetism in Na_4IrO_4 is very localized and different magnetic configurations have only small effects on the band structures. Regardless of the magnetic configuration, our numerical results show that the $5d$ electronic configuration can always be described by $d_{3z^2-r^2}^1, \uparrow d_{3z^2-r^2}^1, \downarrow d_{xz}^1, \uparrow d_{yz}^1, \uparrow d_{xy}^1$. While for most of $5d$ transition metal oxides, the magnetization is quite itinerant and the magnetic configuration strongly affect the band structure [5]. The calculated magnetic moment at Ir site is around $1.35 \mu_B$, considerably small than that of $S = 3/2$ configuration. Due to the strong hybridization between Ir- $5d$ and O- $2p$ states, there is also considerable magnetic moment located at O site. As shown in Table I, the AFM-1 configuration has the lowest total energy. Although we only consider four magnetic configurations, we believe that the AFM-1 is indeed the magnetic ground state configuration as

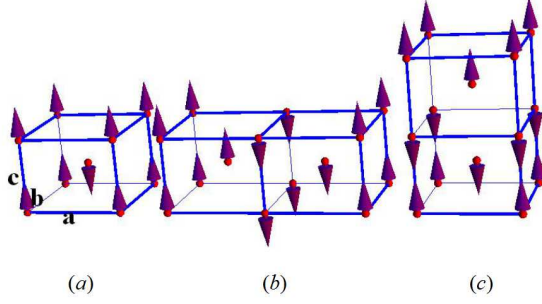


FIG. 4: The AFM magnetic configurations of Na_4IrO_4 which we considered in DFT calculations. For clarity only Ir atoms are shown. (a), (b) and (c) represent AFM-1, AFM-2 and AFM-3 configurations, respectively.

TABLE I: The calculated total energy (in meV) per unit cell and magnetic moments (in μ_B) for the four magnetic configurations from LSDA and LSDA + U ($U = 2$ eV) calculations. The total energy of AFM1 state is set to zero.

	LSDA				LSDA+ U			
	FM	AFM1	AFM2	AFM3	FM	AFM1	AFM2	AFM3
E_{total}	44.5	0	19.7	17.9	22.8	0	10.8	8.4
m_{Ir}	1.40	1.32	1.34	1.35	1.48	1.45	1.46	1.46
m_{O}	0.27	0.25	0.26	0.26	0.26	0.25	0.26	0.26

discussed in the following sections.

As the importance of electronic correlation for 5d orbitals has been recently emphasized [3–5], we utilize the LSDA + U scheme, which is adequate for the magnetically ordered insulating ground states, to consider the electronic correlation in Ir-5d states. The estimates for the values of U have been recently obtained between 1.4 and 2.4 eV in layered Sr_2IrO_4 and Ba_2IrO_4 [31]. The Ir ion in the IrO_4 moiety has only four nearest neighbors. Moreover IrO_4 moieties are highly-isolated, thus we generally expect that the value of U in Na_4IrO_4 is larger than that in other 5d transition metal oxides. We have varied the value of U from 2.0 to 3.0 eV, the electronic structure and magnetic properties depend moderately on U and the numerical calculations show that the essential properties and our conclusions do not depend on the value of U . Thus we only show the results with $U = 2$ eV at follows. Similarly we consider the four magnetic configurations and the results of relative total energies and magnetic moments are also summarized in Table. I while AFM-1 state still has the lowest energy. Including U will enhance the exchange splitting in 5d bands, and slightly enlarge the calculated magnetic moments as shown in Table I. The band structures of Na_4IrO_4 with AFM-1 order from the LSDA + U calculation is presented in Fig. 5.

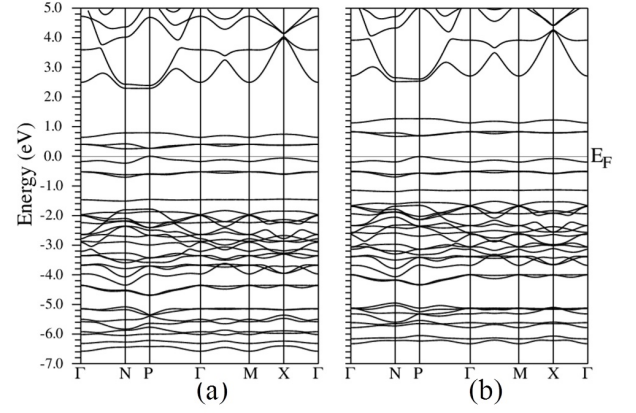


FIG. 5: Band structure of AFM-1 configuration calculated by (a) LSDA (b) LSDA + U ($= 2$ eV) method.

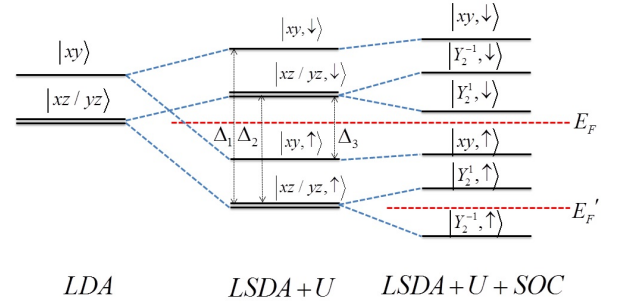


FIG. 6: Schematic picture of orbital occupation around Fermi level. From LDA (left panel), LSDA+ U (middle panel) and LSDA+ U +SOC (right panel) calculations. LSDA calculation has the same pattern with LSDA+ U calculations and is not presented here. E_F represent the Fermi-level of Na_4IrO_4 . As mentioned in the maintext, substituting Ir ions by Re ions, the Fermi-level shifts to E'_F , which significantly enhances the MAE.

The result from the LSDA calculation within the AFM-1 configuration is also shown for comparison. Compared with the LSDA calculation, the bands within LSDA + U scheme are narrower but the order of crystal field splitting pattern and electronic occupation does not change. The LSDA + U calculation predicts a little bigger magnetic moment for Ir ions ($1.45 \mu_B$) and a larger gap of about 0.57 eV, as shown in Table. I and Fig. 5. We also show the d orbital splitting under the crystal field of square plane in the middle panel of Fig. 6, and the electronic occupation pattern is decided by the competition between the crystal field splitting and Hund's rule. It is worth mentioning that the results such as the crystal splitting pattern, are not dependent on the value of U .

The strong SOC in 5d atoms usually significantly affects the band dispersions, thus we also perform the LSDA + U + SOC calculations. Since the IrO_4 moiety is in the ab -plane, we perform the LSDA + U + SOC calculations with spin orientations perpendicular to ab -

plane and lying in ab -plane, i.e. the spin orientations are along (001), (010) and (100) directions. Our calculations show that the (001) is the easy axis and (100) is the hard axis. We list the calculated magnetic moments and total energies in Table II and find that AFM-1 state is still the ground state configuration. Unlike LSDA + U calculations, the degeneracy of d_{xz} and d_{yz} is removed by SOC, as shown in Fig. 7 and the right panel of Fig. 6. The most remarkable feature is the huge MAE. The MAE of Na_4IrO_4 is around 12 meV per Ir atom with the highly preferential easy axis being out of ab -plane. It is easy to see from Table II that for all of the four magnetic configurations, (001) direction is the easy axis and the MAE have the similar values from 11.6 to 12.6 meV per Ir atom.

Large magnetic anisotropy energy (MAE) is desirable for magnetic devices. Recently, there has been considerable research interest in studying materials with a large MAE. Most of them are two dimensional materials or adatoms on surfaces. For example, Co atoms deposited on a Pt (111) surface [38], Fe or Mn atoms absorbed on the CuN surface [39], and Co or Fe atoms on Pd or Rh (111) surface [40]. In addition, Rau et al. [41] found a giant MAE for the Co atoms absorbed on top of the O sites of MgO (001) surface. Generally, the bulk materials exhibit relatively small MAE of a few μeV [42, 43] while anisotropy energies are larger by about three orders of magnitude for multilayers and surface systems [43]. MAE originates from the interaction of the atom's orbital magnetic moment and spin angular momentum, thus an important factor of MAE is the strength of SOC, which increases from $3d$ to $5d$ metals. Another important factor is the special coordination environment, since a ligand field often quenches the orbital moment. Since the IrO_4 in Na_4IrO_4 shows an isolated planar structure, large MAE is expected.

In order to confirm the giant value of MAE, we also calculate the variation of the total energy by changing the magnetization direction with the force theorem. In this case, there is no need to converge a complete self-consistency cycle. The evaluated MAE using force theorem gives the similar values. We try to understand the magnetic properties in following sections.

IV. SPIN MODEL

As shown in Table I, the calculated magnetic moments for the different magnetic configurations are similar, thus the total energy differences between the different magnetic configurations are mainly contributed by the inter-atomic exchange interaction where SOC is not considered. This allows us to estimate the exchange couplings by the energy-mapping analysis (see Appendix). As shown in Fig. 1, we consider three spin exchange paths. J_1 is the nearest-neighbor Ir-Ir exchange coupling along c -axis, J_2 is the next-nearest-neighbor one along diagonal line while J_3 is the 3rd-nearest-neighbor one along

TABLE II: The calculated total energy (in meV) per unit cell and magnetic moments (in μB) for the four magnetic configurations from LSDA + SOC + U ($U = 2$ eV) calculations with (001) and (100) spin orientations. The total energy of AFM-1 state with (001) magnetization direction is set to zero. MAE (in meV) per Ir atom for four magnetic configurations are also summarized in the table.

	FM		AFM-1		AFM-2		AFM-3	
	(001)	(100)	(001)	(100)	(001)	(100)	(001)	(100)
E_{total}	22.3	34.4	0	11.6	11.1	22.8	8.9	21.5
$m_{\text{Ir}}(\text{spin})$	1.37	1.38	1.34	1.35	1.36	1.36	1.36	1.36
$m_{\text{Ir}}(\text{orbital})$	0.11	0.10	0.10	0.10	0.10	0.10	0.10	0.10
m_{O}	0.25	0.24	0.24	0.23	0.24	0.24	0.24	0.24
MAE	12.1		11.6		11.7		12.6	

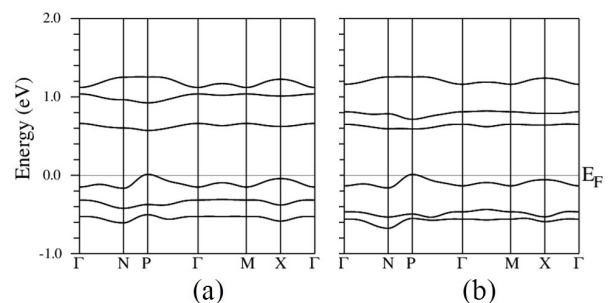


FIG. 7: Band structure of Na_4IrO_4 calculated by the method of LSDA + U + SOC ($U = 2$ eV) calculation. (a) and (b) represent spin orientations along (001) direction and (100) direction, respectively.

a/b -axis. The distance in J_3 (7.1 \AA) is much longer than J_1 (4.7 \AA) and J_2 (5.6 \AA). Compared with LSDA + U , LSDA overestimates the hopping, consequently gives larger exchange parameters as shown in Table III. J_1 , J_2 and J_3 are all AFM. Although J_1 has the nearest-neighbor exchange path, $d_{3z^2-r^2}$ orbital is fully occupied in both up and down spin channel as mentioned in the previous section and the hoppings for the other d orbitals are relatively small. Therefore, it is easy to understand that the value of J_1 is less than J_2 . Thus J_2 dominates over the others in strength, while J_3 is nearly negligible due to the much long distance, as shown in Table III. Although the spin exchange couplings J_1 - J_3 decrease with increasing U values, J_2 is always dominated while J_3 is nearly negligible. The exchange interaction in magnetic insulators is predominantly caused by the so-called superexchange — which is due to the overlap of the localized orbitals of the magnetic electrons with those of intermediate ligands. The Ir-Ir distance in Na_4IrO_4 is very large, thus the value of exchange interaction J with longer distance should be very smaller and have no influence on the magnetic ground state. Thus we believe that the strongest J_2 makes AFM-1 as the ground state, in agreement with the total energy calculations.

Based on the J_1 - J_3 parameters from LSDA + U , we calculate the Curie-Weiss temperature θ and Néel temperature T_N using the mean-field approximation theory[44]. θ is estimated to -105 K while T_N is about 56 K. The values of -105 K and 56 K are both somewhat larger but qualitatively consistent with the experimental ones of -78 K and 25 K, respectively. Since the mean-field approximation theory often overestimate the Curie-Weiss and Néel temperatures, our mapping J_1 - J_3 parameters are thought to be in reasonable agreement with experimental results.

V. MAGNETIC ANISOTROPY ENERGY

In order to understand the origin of the giant MAE, we start from a generalized symmetry allowed spin model of Na_4IrO_4 (See Appendix):

$$H_S = -K \sum_i S_i^{z2} + \frac{1}{2} \sum_{\langle i,j \rangle, \alpha\beta} J_{ij}^{\alpha\beta} S_i^\alpha S_j^\beta, \quad (1)$$

where the first term represents the single ion anisotropy Hamiltonian, the second one is the inter-atomic exchange Hamiltonian, i, j label the Ir ions and α, β take x, y, z . Due to the inversion symmetry, $J_{ij}^{\alpha\beta} = J_{ij}^{\beta\alpha}$, which means there is no Dzyaloshinskii-Moriya interaction [45, 46]. We only consider the exchange neighbors $\langle ij \rangle$'s to the 3rd nearest-neighbor, which are denoted by J_1, J_2, J_3 in order as shown in Fig. 1. For J_1 , due to the C_4 rotation symmetry, $J_1^{\alpha\beta} = \delta_{\alpha\beta} J_1^{\alpha\alpha}$ and $J_1^{xx} = J_1^{yy}$. While for J_2 and J_3 , the non-diagonal terms (i.e. J^{xy}, J^{xz} and J^{yz}) is symmetry-allowed, however these terms are proportional to the product of λ^2 and isotropic exchange [47], and should be very small, thus we ignore them hereafter.

Using the similar energy-mapping method (See Appendix), we estimate the parameters in Eq. (1) and show the results in Table. III. It is clear that the anisotropy of spin exchange is small, especially for the dominating spin exchange, where J_2 shows a small difference between J_2^{xx}, J_2^{yy} and J_2^{zz} . The different spin configurations have almost the same value of MAE, and the anisotropy of spin exchange coupling parameters is little, indicating that MAE is dominated by the single-ion anisotropy.

To understand the origin of single-ion anisotropy, we consider the crystal field splitting, electronic occupation shown in Fig. 6, and the SOC Hamiltonian $\lambda \mathbf{L} \cdot \mathbf{S}$ where λ is the SOC constant. With the spin direction described by the two angles (θ, φ) , where θ and φ are the azimuthal and polar angles of the spin orientation with respect to the local coordinate environment, the $\lambda \mathbf{L} \cdot \mathbf{S}$ term can be written as [48]

TABLE III: Isotropic spin exchange parameters (in meV) and anisotropic spin exchange parameters evaluated by energy-mapping analysis from LSDA, LSDA + U , LSDA + SOC + U ($U = 2$ eV) calculations, respectively.

	LSDA	LSDA+ U	LSDA+ U +SOC		
			J_i^{xx}	J_i^{yy}	J_i^{zz}
J_1/meV	0.97	0.66	0.32	0.32	0.51
J_2/meV	2.47	1.27	1.21	1.35	1.24
J_3/meV	0.56	0.14	0.02	0.02	0.01
K/meV	-	-	5.4		

$$\begin{aligned}
H_{so} = & \lambda \hat{S}_z' (\hat{L}_z \cos \theta + \frac{1}{2} \hat{L}_+ e^{-i\varphi} \sin \theta + \frac{1}{2} \hat{L}_- e^{i\varphi} \sin \theta) \\
& + \frac{\lambda}{2} \hat{S}_{+}' (-\hat{L}_z \sin \theta - \hat{L}_+ e^{-i\varphi} \sin^2 \frac{\theta}{2} + \hat{L}_- e^{i\varphi} \cos^2 \frac{\theta}{2}) \\
& + \frac{\lambda}{2} \hat{S}_{-}' (-\hat{L}_z \sin \theta + \hat{L}_+ e^{-i\varphi} \cos^2 \frac{\theta}{2} + \hat{L}_- e^{i\varphi} \sin^2 \frac{\theta}{2})
\end{aligned} \quad (2)$$

Using perturbation theory by treating the SOC Hamiltonian as the perturbation combined with the d orbital occupation pattern, we can get the associated energy lowering:

$$\begin{aligned}
\Delta E^{(1)} &= \sum_i \langle i | H_{so} | i \rangle \\
\Delta E^{(2)} &= - \sum_{i,j} \frac{|\langle i | H_{so} | j \rangle|^2}{|e_i - e_j|}
\end{aligned} \quad (3)$$

where i represents an occupied d -level state with energy e_i while j represents an unoccupied d -level state with energy e_j , and the third and higher order perturbations are not given here. In Na_4IrO_4 , where the SOC has not been considered, $d_{xz,\uparrow}$ and $d_{yz,\uparrow}$ are doubly-degenerate. We can see that the degeneracy of $d_{xz,\uparrow}$ and $d_{yz,\uparrow}$ is lifted by the SOC and they split to $|Y_2^1, \uparrow\rangle$ and $|Y_2^{-1}, \uparrow\rangle$. The splitting is $\pm \frac{\lambda}{2} |\cos \theta|$ according to the first order perturbation, thus the splitting for the spin polarization of (001) direction is larger than that for (100) direction, as shown in Fig. 7. However, the $d_{xy,\uparrow}, d_{xz,\uparrow}$ and $d_{yz,\uparrow}$ are fully occupied and the band gap is quite big with respect to the SOC constant λ . Thus the first order perturbation is negligible and has no contribution to the single-ion anisotropy.

Therefore, we consider the second order perturbation. Note that in the common 5d transition metal oxides with face (or edge, corner)-sharing structure of oxygen octahedrons, the widths of the t_{2g} -block bandwidths are relatively large while the $|e_i - e_j|$ values are relatively small, so the perturbation theory does not lead to an accurate estimation of MAE. But in Na_4IrO_4 , the widths of the bands around Fermi-level are about 0.2 eV and the $|e_i - e_j|$ value is around ~ 2 eV, thus one can get the

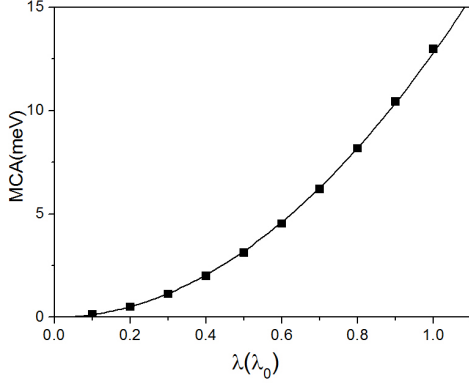


FIG. 8: SOC strength dependence of the magnetic anisotropy energy of Na_4IrO_4 calculated by the method of LSDA + SOC + U ($U = 2$ eV).

quantitative value of MAE more accurately by the second order perturbation

$$E = -\lambda^2 \cos^2 \theta \left[\frac{1}{4\Delta_1} + \frac{1}{4\Delta_3} - \frac{1}{2\Delta_2} \right] \quad (4)$$

Here Δ_i is the splitting of on-site d -orbital energy levels, as shown in Fig. 6. The orbitals of $d_{x^2-y^2}$ and d_{z^2} are far away from the Fermi-level and can be ignored. From the LSDA + U ($U = 2$ eV) calculations, we estimate the orbital energy levels by the weight-center positions of DOS and get the values of Δ_i . The calculated values of Δ_1 , Δ_2 and Δ_3 are 1.82, 1.35 and 0.89 eV, respectively. Using these value of Δ_i and $\lambda = 0.5$ eV, we get the MAE as 12.0 meV, consistent with the value directly from DFT theory. Thus the second order perturbation is dominant in MAE and higher order perturbations are believed to be little. One reason of the giant MAE is the SOC strength, which is very strong for $5d$ electrons. It is about 3 times as high as $4d$ electrons and an order of magnitude higher than $3d$ electrons. Besides the strong SOC strength, the d -level splitting is also a significant cause of the giant MAE. The d -level splitting condition comes from the special square planar local environment which indicates a giant anisotropy between in-plane and out-of-plane. The long distances of IrO_4 moieties make the strong local magnetization. These factors together make the giant value of MAE.

We also calculate MAE with varying the SOC strength λ within LSDA + U + SOC scheme. As shown in Fig. 8, it is obviously that the MAE of Na_4IrO_4 is nearly proportional to the square of λ , in accordance with Eqn. (4).

Using the calculated spin model parameters, one can obtain the magnon spectrum on the basis of the Holstein-Primakoff transformation and the Fourier transformation. We calculate the spin-wave dispersion along high-symmetry axis and display the result in Fig. 9. As shown

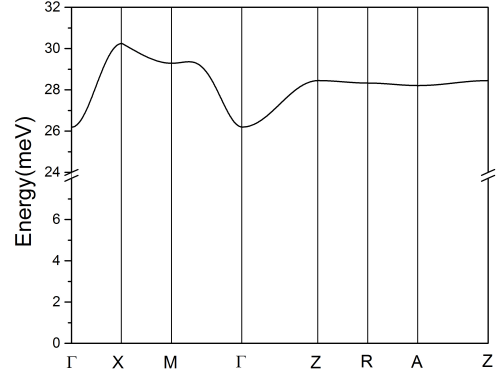


FIG. 9: Calculated spin-wave dispersion curves along high-symmetry axis for the Na_4IrO_4 .

in Fig. 9, there is a large spin gap of about 26 meV while the width of spin-wave dispersion is only 4 meV. This is due to the large single-ion anisotropy and relatively small exchange couplings.

VI. MATERIAL DESIGN

As shown in Fig. 6, for Na_4IrO_4 , the exchange splitting is large and there is a relatively big gap between occupied and unoccupied states. Therefore the first order perturbation of SOC is very small. We expect that if the Fermi-level shifts to the position of E'_F as shown in Fig. 6, there is nonzero first order term and the MAE will be enhanced significantly. We try to realize the Fermi-level shift through substituting Ir ions in Na_4IrO_4 by Re ions. The MAE of Na_4ReO_4 may be even larger and it may reach the limit of MAE even in bulk materials, with the same size as Co or other atoms absorbed on top of the O sites of MgO (001) surface [36, 37].

In order to examine the dynamic stability, we calculate phonon spectrum of Na_4ReO_4 (See Appendix), and show the calculated phonon spectrum along high-symmetry lines in Fig. 10. All the phonon modes of Na_4ReO_4 are positive, indicating the structure is dynamically stable.

The calculated value of MAE is about 140 meV per Ir atom. It can be explained by the same method using perturbation theory, where Na_4ReO_4 have two less occupied electrons. For Na_4ReO_4 , with the absence of SOC interaction, the orbitals of $d_{xz,\uparrow}$ and $d_{yz,\uparrow}$ are doubly-degenerate and half-occupied. With the presence of SOC, the doubly-degenerate $d_{xz,\uparrow}/d_{yz,\uparrow}$ bands split to $|Y_2^1, \uparrow\rangle$ and $|Y_2^{-1}, \uparrow\rangle$, where $|Y_2^{-1}, \uparrow\rangle$ is fully occupied while $|Y_2^1, \uparrow\rangle$ is fully unoccupied. Thus the first order perturbation of total energy can be written as:

$$E = -\frac{\lambda}{2} |\cos \theta| \quad (5)$$

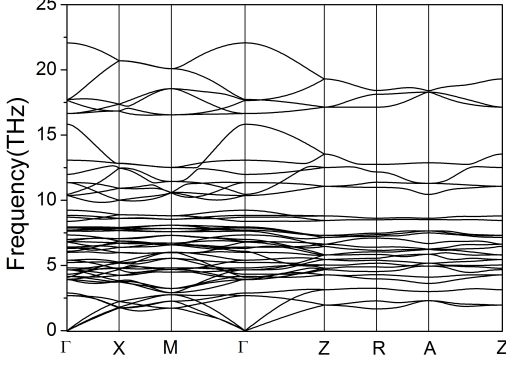


FIG. 10: Calculated phonon dispersion for Na_4ReO_4 .

The calculated MAE of 140 meV is in good agreement with the expected value of $\frac{\lambda}{2}$, as the SOC strength λ of the $5d$ electrons is generally regarded as $0.3\sim 0.5$ eV.

VII. CONCLUSIONS

In conclusion, using first-principles and perturbation theory, we present a comprehensive investigation of the $5d$ transition-metal oxides Na_4IrO_4 , where Ir occupies the center of square-planar coordination environment. We discuss its electronic structures, determine its magnetic ground state configuration, and find a giant MAE for this compound. We clarify the microscopic mechanism about this novel magnetic properties, and also suggest possible way to further enhance MAE. We expect that the $5d$ transition metal oxides with low symmetry and long $5d$ - $5d$ distance may exhibit extraordinarily large coercive fields. The prediction about giant MAE deserves experimental tests and may provide a route to nanoscale magnetic devices.

This work was supported by the Ministry of Science and Technology of China (Grant number: 2017YFA0303200), NSFC under Grants No. 11525417 and No. 11374137.

VIII. APPENDIX

A. Symmetry analysis

Symmetry will add some restrictions on the magnetic model. Considering the time reversal symmetry and to the quadratic terms of spins, the magnetic model can be written in the following general form:

$$H = \frac{1}{2} \sum_{ls, l's'} S_{ls}^\dagger J(ls, l's') S_{l's'}, \quad (6)$$

where S_{ls} represents the magnetic moment located at the magnetic ion labeled by s in the l th unit cell. $J(ls, l's')$ is the exchange interaction between S_{ls} and $S_{l's'}$. It is obviously a 3×3 real matrix, because the magnetic moment is a three-component vector and we adopt the conventional Cartesian coordinate system. Translation symmetry will restrict $J(ls, l's')$ to be related to $l' - l$, irrespective of the starting unit cell. Rotation inversion or the combination of two will also give some restrictions on the exchange matrix. Considering a general space group element, $\{\alpha|\mathbf{t}\}$, of which α is the point operation, we denote the representation matrix as $R(\alpha)$ of α in the coordinate system here. Then $J(ls, l's')$ should satisfy that,

$$R(\alpha)^\dagger J(mp, m'p') R(\alpha) = J(ls, l's'), \quad (7)$$

where mp and $m'p'$ are related to ls and $l's'$ by the action of $\{\alpha|\mathbf{t}\}$, respectively.

We then get ready to turn to the magnetic model for Na_4IrO_4 . Because there is only one magnetic ion, namely Ir, in one unit cell, we can just label the magnetic moment by the unit cell label l . Utilizing the translation property, we just need to consider $J(0, l)$, which we denote to be $J(l)$ or $J(l_1, l_2, l_3)$ hereafter. The onsite exchange $J(0, 0, 0)$ is found to own the following form,

$$J(0, 0, 0) = \begin{pmatrix} J(0, 0, 0)_{11} & 0 & 0 \\ 0 & J(0, 0, 0)_{11} & 0 \\ 0 & 0 & J(0, 0, 0)_{33} \end{pmatrix}, \quad (8)$$

which represent the single ion anisotropy $\sim S_z^2$.

According to the lattice parameters, we find that $l = (0, 0, 1)$ and $(0, 0, -1)$ are for the nearest-neighborhoods, $l = (\eta_1 1/2, \eta_2 1/2, \eta_3 1/2)$ ($\eta_i = \pm$) for the eight next-nearest-neighborhoods, and $l = (\pm 1, 0, 0), (0, \pm 1, 0)$ for the 3rd-nearest-neighborhoods.

Then $J(0, 0, \pm 1)$ are found to be in the following form:

$$J(0, 0, \pm 1) = \begin{pmatrix} J(0, 0, 1)_{11} & 0 & 0 \\ 0 & J(0, 0, 1)_{11} & 0 \\ 0 & 0 & J(0, 0, 1)_{33} \end{pmatrix}, \quad (9)$$

and note that in the maintext, we relabel $J(0, 0, 1)_{11}$ and $J(0, 0, 1)_{22}$ to be J_1^{xx} and J_1^{yy} , respectively.

For the next-nearest-neighborhoods, inversion symmetry will restrict $J(1/2, 1/2, 1/2)$ to be a symmetric matrix, which would allow finite non-diagonal elements. However we can ignore these symmetric non-diagonal elements, because physically they are relatively small [47]. Then the $J(\eta_1 1/2, \eta_2 1/2, \eta_3 1/2)$ are in the following form,

$$J(\eta_1 1/2, \eta_1 1/2, \pm 1/2) = \begin{pmatrix} J(1/2, 1/2, 1/2)_{11} & 0 & 0 \\ 0 & J(1/2, 1/2, 1/2)_{22} & 0 \\ 0 & 0 & J(1/2, 1/2, 1/2)_{33} \end{pmatrix}, \quad (10)$$

$$J(\eta_1 1/2, -\eta_1 1/2, \pm 1/2) = \begin{pmatrix} J(1/2, 1/2, 1/2)_{22} & 0 & 0 \\ 0 & J(1/2, 1/2, 1/2)_{11} & 0 \\ 0 & 0 & J(1/2, 1/2, 1/2)_{33} \end{pmatrix}, \quad (11)$$

and note that in the main text, we relabel $J(1/2, 1/2, 1/2)_{11}$, $J(1/2, 1/2, 1/2)_{22}$, and $J(1/2, 1/2, 1/2)_{33}$ to be J_2^{xx} , J_2^{yy} and J_2^{zz} , respectively.

Finally $J(\pm 1, 0, 0)$ and $J(0, \pm 1, 0)$ are found to be in the following form:

$$J(\pm 1, 0, 0) = \begin{pmatrix} J(1, 0, 0)_{11} & J(1, 0, 0)_{12} & 0 \\ J(1, 0, 0)_{12} & J(1, 0, 0)_{22} & 0 \\ 0 & 0 & J(1, 0, 0)_{33} \end{pmatrix}, \quad (12)$$

$$J(0, \pm 1, 0) = \begin{pmatrix} J(1, 0, 0)_{22} & -J(1, 0, 0)_{12} & 0 \\ -J(1, 0, 0)_{12} & J(1, 0, 0)_{11} & 0 \\ 0 & 0 & J(1, 0, 0)_{33} \end{pmatrix}, \quad (13)$$

and note that in the main text, we relabel $J(1, 0, 0)_{11}$, $J(1, 0, 0)_{22}$ and $J(1, 0, 0)_{33}$ to be J_3^{xx} , J_3^{yy} and J_3^{zz} , respectively. The non-diagonal elements $J(1, 0, 0)_{12}$ are still thought to be very small and ignored [47].

B. Energy-mapping analysis

We evaluate spin exchange parameters J_1 - J_3 by energy-mapping analysis. Firstly we consider four magnetic configurations as shown in Fig. 4. The total energies of these four spin states can be described in terms of the spin Hamiltonian:

$$H = \sum_{i < j} J_{ij} \hat{S}_i \cdot \hat{S}_j \quad (14)$$

where J_{ij} ($= J_1, J_2, J_3$) is the spin exchange parameter between the spin sites i and j . By applying the energy expressions obtained for a spin dimer with $S = 3/2$ for Ir^{4+} ions, the total energies per unit cell for these four spin configurations are expressed as

$$E_{FM} = (2J_1 + 8J_2 + 4J_3) \left(\frac{S^2}{2} \right) \quad (15)$$

$$E_{AFM1} = (2J_1 - 8J_2 + 4J_3) \left(\frac{S^2}{2} \right) \quad (16)$$

$$E_{AFM2} = 2J_1 \times \left(\frac{S^2}{2} \right) \quad (17)$$

$$E_{AFM3} = (-2J_1 + 4J_3) \left(\frac{S^2}{2} \right) \quad (18)$$

The relative energies of the four spin states are obtained from LSDA and LSDA + U ($U = 2$ eV) calculations and the values of J_1 to J_3 can be evaluated by mapping these energies. The calculated magnetic moments for the four magnetic configurations have little difference, as shown in Table. I. The calculated spin exchange coupling parameters J_1 to J_3 are summarized in Table. III. The spin exchanges J_1 , J_2 and J_3 are all AFM and J_2 dominates over others in strength, while J_3 is almost negligible.

Considering a generalized symmetry allowed spin model described in Eq. (1), which includes the anisotropic part of J and single-ion anisotropy, the values of J^{xx} , J^{yy} , J^{zz} and K can be determined by energy-mapping analysis of LSDA + U + SOC calculations with different magnetization directions. In order to estimate these values, one more magnetic configuration should be considered, as shown in Fig. 11. The total energies per unit cell with different magnetic configurations are expressed as

$$E_{FM}^{(001)} = (2J_1^{zz} + 8J_2^{zz} + 4J_3^{zz})\left(\frac{S^2}{2}\right) - KS^2 \quad (19)$$

$$E_{AFM1}^{(001)} = (2J_1^{zz} - 8J_2^{zz} + 4J_3^{zz})\left(\frac{S^2}{2}\right) - KS^2 \quad (20)$$

$$E_{AFM2}^{(001)} = 2J_1^{zz} \times \left(\frac{S^2}{2}\right) - KS^2 \quad (21)$$

$$E_{AFM3}^{(001)} = (-2J_1^{zz} + 4J_3^{zz})\left(\frac{S^2}{2}\right) - KS^2 \quad (22)$$

$$E_{AFM4}^{(001)} = (2J_1^{zz} - 4J_3^{zz})\left(\frac{S^2}{2}\right) - KS^2 \quad (23)$$

$$E_{FM}^{(100)} = (2J_1^{xx} + 4J_2^{xx} + 4J_2^{yy} + 2J_3^{xx} + 2J_3^{yy})\left(\frac{S^2}{2}\right) \quad (24)$$

$$E_{AFM1}^{(100)} = (2J_1^{xx} - 4J_2^{xx} - 4J_2^{yy} + 2J_3^{xx} + 2J_3^{yy})\left(\frac{S^2}{2}\right) \quad (25)$$

$$E_{AFM2}^{(100)} = (2J_1^{xx} + 2J_3^{xx} - 2J_3^{yy})\left(\frac{S^2}{2}\right) \quad (26)$$

$$E_{AFM3}^{(100)} = (-2J_1^{xx} + 2J_3^{xx} + 2J_3^{yy})\left(\frac{S^2}{2}\right) \quad (27)$$

$$E_{AFM4}^{(100)} = (2J_1^{xx} - 4J_2^{xx} + 4J_2^{yy} - 2J_3^{xx} - 2J_3^{yy})\left(\frac{S^2}{2}\right) \quad (28)$$

$$E_{FM}^{(010)} = (2J_1^{xx} + 4J_2^{xx} + 4J_2^{yy} + 2J_3^{xx} + 2J_3^{yy})\left(\frac{S^2}{2}\right) \quad (29)$$

$$E_{AFM1}^{(010)} = (2J_1^{xx} - 4J_2^{xx} - 4J_2^{yy} + 2J_3^{xx} + 2J_3^{yy})\left(\frac{S^2}{2}\right) \quad (30)$$

$$E_{AFM2}^{(010)} = (2J_1^{xx} - 2J_3^{xx} + 2J_3^{yy})\left(\frac{S^2}{2}\right) \quad (31)$$

$$E_{AFM3}^{(010)} = (-2J_1^{xx} + 2J_3^{xx} + 2J_3^{yy})\left(\frac{S^2}{2}\right) \quad (32)$$

$$E_{AFM4}^{(010)} = (2J_1^{xx} + 4J_2^{xx} - 4J_2^{yy} - 2J_3^{xx} - 2J_3^{yy})\left(\frac{S^2}{2}\right) \quad (33)$$

The relative total energies of these spin states are obtained from LSDA + U + SOC calculations, which are summarized in Table. IV. The calculated magnetic moments for these magnetic configurations have

little difference, as also summarized in Table. IV. By energy-mapping analysis, the calculated anisotropic spin exchange coupling parameters $J_i^{\alpha\alpha}$ and single-ion anisotropy parameter K are summarized in Table. III.

C. Details of results for Na_4ReO_4

The phonon calculation is performed from the finite displacement method as implemented in the Vienna ab-initio simulation package (VASP) [32–34] and the PHONOPY package [35]. After a series of tests, a

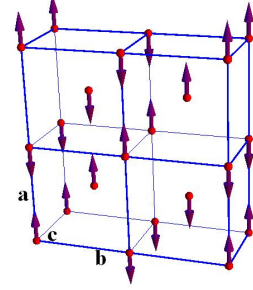


FIG. 11: The AFM-4 magnetic configuration of Na_4IrO_4 . For clarity only Ir atoms are shown.

$3 \times 3 \times 2$ supercell is constructed to ensure the force convergence, and a $2 \times 2 \times 4$ k-mesh for the Brillouin zone sampling is used in the phonon calculation. The calculated phonon spectrum along high-symmetry lines is shown in Fig. 10.

In Na_4ReO_4 case, Re^{4+} ion has two less occupied 5d electrons than Ir^{4+} ion. We perform first-principles calculations and find that the crystal field splitting does not change. The calculated magnetic moment is $0.51 \mu_B$. We perform several calculations for different magnetic configurations and find that the magnetic ground-state configuration is the FM state. The calculated spin exchange coupling parameters J_1 to J_3 are -1.84 meV, -0.84 meV and -0.04 meV, respectively. However, the single-ion anisotropy has a overwhelmingly major contribution on MAE especially in Na_4ReO_4 , which has an order of magnitude larger single-ion anisotropy than Na_4IrO_4 .

-
- [1] M. Imada, A. Fujimori, and Y. Tokura, Rev. Mod. Phys. **70**, 1039 (1998).
 - [2] G. Kotliar, S. Y. Savrasov, K. Haule, V. S. Oudovenko, O. Parcollet, and C. A. Marianetti, Rev. Mod. Phys. **78**, 865 (2006).
 - [3] W. Witczak-Krempa, G. Chen, Y. B. Kim, and L. Balents, Annu. Rev. Condensed Matter Physics **5**, 57 (2013).
 - [4] J. G. Rau, E. K.-H. Lee, and H.-Y. Kee, Annu. Rev.

- Condensed Matter Physics **7**, 195 (2016).
- [5] Y. Du and X. Wan, Computational Mater. Sci. **112**, 416 (2016).
- [6] B. J. Kim et al., Phys. Rev. Lett. **101**, 076402 (2008); B. J. Kim et al., Science **323**, 1329 (2009).
- [7] H. Jin, H. Jeong, T. Ozaki, J. Yu, Phys. Rev. B **80**, 075112 (2009).
- [8] H. Watanabe, T. Shirakawa, S. Yunoki, Phys. Rev. Lett. **105**, 216410 (2010).

TABLE IV: The calculated total energy (in meV) per unit cell and magnetic moments (in μ_B) for the four magnetic configurations from LSDA + SOC + U ($U = 2$ eV) calculations with (001), (010) and (100) spin orientations for energy-mapping analysis.

	FM			AFM-1			AFM-2			AFM-3			AFM-4		
	(001)	(100)	(010)	(001)	(100)	(010)	(001)	(100)	(010)	(001)	(100)	(010)	(001)	(100)	(010)
E_{total}	22.3	34.4	34.4	0	11.6	11.6	11.1	22.8	22.8	8.9	21.5	21.5	10.9	23.3	21.7
$m_{Ir}(\text{spin})$	1.37	1.38	1.38	1.34	1.35	1.35	1.36	1.36	1.36	1.36	1.36	1.36	1.36	1.36	1.36
$m_{Ir}(\text{orbital})$	0.11	0.10	0.10	0.10	0.10	0.10	0.10	0.10	0.10	0.10	0.10	0.10	0.10	0.10	0.10
m_O	0.25	0.24	0.24	0.24	0.23	0.23	0.24	0.24	0.24	0.24	0.24	0.24	0.24	0.24	0.24

- [9] A. Shitade, H. Katsura, J. Kuneš, X.-L. Qi, S.-C. Zhang, N. Nagaosa, Phys. Rev. Lett. **102**, 256403 (2009).
- [10] D.A. Pesin, L. Balents, Nat. Phys. **6**, 376 (2010).
- [11] C. H. Kim, H. S. Kim, H. Jeong, H. Jin, and J. Yu, Phys. Rev. Lett. **108**, 106401 (2012).
- [12] G. Jackeli, G. Khaliullin, Phys. Rev. Lett. **102**, 017205 (2009); J. Chaloupka, G. Jackeli, and G. Khaliullin, Phys. Rev. Lett. **105**, 027204 (2010).
- [13] X. Wan, A. M. Turner, A. Vishwanath, and S. Y. Savrasov, Phys. Rev. B **83**, 205101 (2011).
- [14] F. Wang, T. Senthil, Phys. Rev. Lett. **106**, 136402 (2011).
- [15] X. Wan, A. Vishwanath, S.Y. Savrasov, Phys. Rev. Lett. **108**, 146601 (2012).
- [16] T. Okamoto, M. Nohara, H. Aruga-Katori, H. Takagi, Phys. Rev. Lett. **99**, 137207 (2007).
- [17] P.A. Lee, Science **321**, 1306 (2008); L. Balents, Nature **464**, 199 (2010).
- [18] D. Mandrus, J. R. Thompson, R. Gaal, L. Forro, J. C. Bryan, B. C. Chakoumakos, L. M. Woods, B. C. Sales, R. S. Fishman, and V. Keppens, Phys. Rev. B **63**, 195104 (2001); W. J. Padilla, D. Mandrus, and D. N. Basov, Phys. Rev. B **66**, 035120 (2002).
- [19] Y. G. Shi, Y. F. Guo, S. Yu, M. Arai, A. A. Belik, A. Sato, K. Yamaura, E. Takayama-Muromachi, H. F. Tian, H. X. Yang, J. Q. Li, T. Varga, J. F. Mitchell, and S. Okamoto, Phys. Rev. B **80**, 161104 (2009).
- [20] Y. Du, X. Wan, L. Sheng, J. Dong, and S. Y. Savrasov, **85**, 174424 (2012); M.-C. Jung, Y.-J. Song, K.-W. Lee, and W. E. Pickett, Phys. Rev. B **87**, 115119 (2013).
- [21] Y. Shi, Y. Guo, X. Wang, A. J. Princep, D. Khalyavin, P. Manuel, Y. Michiue, A. Sato, K. Tsuda, S. Yu, M. Arai, Y. Shirako, M. Akaogi, N. Wang, K. Yamaura, and A. T. Boothroyd, Nature Mat. **12**, 1024 (2013).
- [22] H. Sim and B. G. Kim, Phys. Rev. B **89**, 201107(R) (2014); H. J. Xiang, Phys. Rev. B **90**, 094108 (2014); H. M. Liu, Y. P. Du, Y. L. Xie, J.-M. Liu, C.-G. Duan, and X. Wan, Phys. Rev. B **91**, 064104 (2015).
- [23] R. Comin, G. Levy, B. Ludbrook, Z.-H. Zhu, C. N. Veenstra, J. A. Rosen, Y. Singh, P. Gegenwart, D. Stricker, J. N. Hancock, D. van der Marel, I. S. Elfimov, and A. Damascelli, Phys. Rev. Lett. **109**, 266406 (2012).
- [24] K. Mader, R. Hoppe, Z. Anorg. Allg. Chem. **619**, 1647 (1993).
- [25] S. Kanungo, B. Yan, P. Merz, C. Felser, and M. Jansen, Angew. Chem. **127**, 5507 (2015).
- [26] P. Blaha, K. Schwarz, G. K. H. Madsen, D. Kvasnicka, and J. Luitz, WIEN2K, An Augmented Plane Wave+ Local Orbitals Program for Calculating Crystal Properties (Karlheinz Schwarz, Technische Universität Wien, Austria, 2001).
- [27] J. Kuneš, T. Jeong, and W. E. Pickett, Phys. Rev. B **70**, 174510 (2004); D. J. Singh, J. Appl. Phys. **79**, 4818 (1996); A. T. Zayak, X. Huang, J. B. Neaton, and K. M. Rabe, Phys. Rev. B **77**, 214410 (2008); X. Wan, J. Zhou, and J. Dong, Europhys. Lett. **92**, 57007 (2010).
- [28] D. D. Koelling and B. N. Harmon, J. Phys. C **10**, 3107 (1977).
- [29] V. I. Anisimov, F. Aryasetiawan, and A. I. Lichtenstein, J. Phys. Condens. Matter **9**, 767 (1997).
- [30] B. J. Kim, H. Ohsumi, T. Komesu, S. Sakai, T. Morita, H. Takagi, and T. Arima, Science **323**, 1329 (2009).
- [31] R. Arita, J. Kuneš, A.V. Kozhevnikov, A.G. Eguiluz, and M. Imada, Phys. Rev. Lett. **108**, 086403 (2012).
- [32] G. Kresse and J. Furthmüller, Comput. Mater. Sci. **6**, 15 (1996).
- [33] G. Kresse and J. Furthmüller, Phys. Rev. B **54**, 11169 (1996).
- [34] G. Kresse and D. Joubert, Phys. Rev. B **59**, 1758 (1999).
- [35] A. Togo, F. Oba and I. Tanaka, Phys. Rev. B **78**, 134106 (2008).
- [36] I. G. Rau, S. Baumann, S. Rusponi, F. Donati, S. Stepanow, L. Gragnaniello, J. Dreiser, C. Piamonteze, F. Nolting, S. Gangopadhyay, O. R. Albertini, R.M. Macfarlane, C. P. Lutz, B. A. Jones, P. Gambardella, A. J. Heinrich, and H. Brune, Science **344**, 988 (2014).
- [37] X. Ou, H. Wang, F. Fan, Z. Li, and H. Wu, Phys. Rev. Lett. **115**, 257201 (2015).
- [38] P. Gambardella, S. Rusponi, M. Veronese, S. S. Dhesi, C. Grazioli, A. Dallmeyer, I. Cabria, R. Zeller, P. H. Dederichs, K. Kern, C. Carbone, and H. Brune, Science **300**, 1130 (2003).
- [39] C. F. Hirjibehedin, C. Y. Lin, A. F. Otte, M. Ternes, C. P. Lutz, B. A. Jones, and A. J. Heinrich, Science **317**, 1199 (2007).
- [40] P. Blonski, A. Lehnert, S. Denmler, S. Rusponi, M. Etzkorn, G. Moulas, P. Bencok, P. Gambardella, H. Brune, and J. Hafner, Phys. Rev. B **81**, 104426 (2010).
- [41] I. G. Rau, S. Baumann, S. Rusponi, F. Donati, S. Stepanow, L. Gragnaniello, J. Dreiser, C. Piamonteze, F. Nolting, S. Gangopadhyay, O. R. Albertini, R.M. Macfarlane, C. P. Lutz, B. A. Jones, P. Gambardella, A. J. Heinrich, and H. Brune, Science **344**, 988 (2014).
- [42] G. H. O. Daalderop, P. J. Kelly, and M. F. H. Schuurmans, Phys. Rev. B **41**, 11919 (1990).
- [43] R. Wu and A. J. Freeman, J. Magn. Magn. Mater. **200**, 498 (1999).
- [44] J. Samuel Smart, Effective Field Theories of Magnetism

- (W. B. Saunders Company, 1966).
- [45] I. Dzyaloshinskii, *Journal of Physics and Chemistry of Solids* **4**, 241 (1958).
- [46] T. Moria, *Physical Review* **120**, 91 (1960).
- [47] M-H Whangbo, H-J Koo, and Dadi Dai, *Journal of Solid State Chemistry* **176**, 417 (2003).
- [48] D. Dai, H. J. Xiang, and M.-H. Whangbo, *J. Comput. Chem.* **29**, 13 (2008).